Supporting Information

A Structural Model for a Self-Assembled Nanotube Provides Insight into Its Exciton Dynamics

Min Gao, Subhradip Paul, Charles D. Schwieters, Zhi-Qiang You, Hui Shao,
John M. Herbert, Jon R. Parquette, and Christopher P. Jaroniec

NMR Spectroscopy

NMR spectra were recorded on a 500 MHz Varian spectrometer equipped with triple-resonance 3.2 mm T3 and BioMAS probes. The MAS rates ranged between 8-11 kHz ± 5 Hz for the different experiments and the sample temperature was regulated at ~10 ºC. Spectra were processed using NMRPipe[1] and analyzed using nmrglue.[2]

Intramolecular ^{13}C-^{13}C distances involving the lysine headgroup ^{13}C′ atoms were measured using the diluted nanotube sample and the rotational resonance width (R^2W) experiment with a 40 ms ^{13}C-^{13}C dipolar mixing period.[3] Two R^2W datasets were recorded, each consisting of a series of 2D ^{13}C-^{13}C spectra with different MAS frequencies. For one of the datasets the spinning frequency was varied in the range 9100 to 9700 Hz containing the ^{13}C′-^{13}Cγ/^{13}Cδ $n = 2$ R^2 matching conditions,[4] while for the other the spinning frequency was varied in the 8300 to 8700 Hz interval containing the ^{13}C′-^{13}Cε $n = 2$ R^2 condition. The proton decoupling throughout the experiments was 83 kHz TPPM.[5]

Intramolecular ^{13}C-^{15}N distances were determined using the diluted nanotube sample and the z-filtered transferred echo double resonance (TEDOR) pulse scheme[6] at 11.111 kHz MAS. The experiment consisted of a set of 2D ^{15}N-^{13}C chemical shift correlation spectra recorded as a function of the TEDOR mixing time up to 12.96 ms, and utilized 27.8 kHz 180º ^{15}N recoupling pulses phased according to the *xy*-4 scheme.[7] The proton decoupling was 100 kHz TPPM during TEDOR mixing and 71 kHz TPPM during the indirect and direct dimensions.

Intermolecular ^{13}C-^{15}N distances were measured using the mixed nanotube sample and band-selective TEDOR[6] at 11.111 kHz. Three separate 1D TEDOR experiments with mixing times up to 21.6 ms were used to probe the K1C′-Nα, K1Cα-Nα and K1Cε-Nζ dipolar couplings after first confirming using a 2D ^{15}N-^{13}C z-filtered TEDOR spectrum with an 18 ms mixing time that for each ^{13}C the correlations arise only from one type of ^{15}N spin (either Nα or Nζ). The proton decoupling was 100 kHz TPPM during TEDOR mixing and 71 kHz TPPM during acquisition.

Extraction of ^{13}C-^{13}C and ^{13}C-^{15}N Distances from NMR Data

In order to extract the ^{13}C-^{13}C distances from the R^2W datasets the intensities of cross-peaks between the C′ and Cγ, Cδ or Cε nuclei were normalized with respect to the intensity of the C′ diagonal peak in a reference spectrum recorded at a similar MAS frequency but sufficiently removed from any $n = 2$ rotational resonance condition. Subsequently, the SPINEVOLUTION[8] software package was used to generate a series of simulated R^2W profiles as a function of the ^{13}C-^{13}C distance in the range of 1 to 7 Å and the zero-quantum transverse relaxation time constant (T_2^{ZQ}) in the range of 1 to 5 ms as described previously,[3] and to fit the experimental R^2W data to these simulated profiles. For increased efficiency, the simulations used for the fitting of the experimental R^2W profiles considered only two coupled ^{13}C spins as opposed to the entire lysine backbone and side-chain topology after confirming that the inclusion of additional ^{13}C spins had negligible effect on the simulations, and also included typical ^{13}C chemical shift anisotropy parameters.[9] Uncertainties in the ^{13}C-^{13}C distances were obtained at the 95% confidence level using an *F*-test.[3]

The intramolecular ^{13}C-^{15}N distances were extracted from the z-filtered TEDOR spectra by fitting the experimental cross-peak buildup trajectories to simulated profiles generated using the analytical model based on the zeroth-order Bessel function approximation.[6] The uncertainties in the intramolecular ^{13}C-^{15}N distances were set at ±15% due to the use of the approximate model as discussed in detail previously.[6] An analogous analytical model for an isolated spin pair was used to obtain the intermolecular ^{13}C-^{15}N distances from band-selective TEDOR buildup trajectories in combination with control experiments that account for the effective ^{13}C transverse relaxation rate and overall amplitude scaling as described in earlier studies,[10] with the uncertainties also set at ±15% due to the use of the two-spin approximation.

Calculation of X-Ray Powder Diffraction Patterns

X-ray powder diffraction (XRD) patterns for the nanotube structural models were calculated within the debyer program (http://code.google.com/p/debyer/) according to the well-known Debye scattering equation:[11]

$$I(q) = \sum_{i,j} f_i f_j \frac{\sin(qr_{ij})}{qr_{ij}}$$

where f_i and f_j are atomic scattering factors, r_{ij} is the distance between atoms i and j, and q is the scattering vector, $q = 4\pi \sin(\theta)/\lambda$, which is related to the wavelength of the incident radiation, λ, and the scattering angle, 2θ. The calculations used as the input λ = 1.5418 Å corresponding to the CuK_α radiation used in previous XRD experiments on NDI-Lys nanotubes,[12] and coordinate files generated in Xplor-NIH with the hydrogen atoms removed. The removal of protons dramatically increased the speed of the calculations with virtually no effect on the calculated XRD patterns due to the small scattering factor for hydrogen.

Structure Calculations

The structure calculation protocol consisted of variable-step-size dynamics for the smaller of 10 ps or 5000 steps at 3,000 K followed by simulated annealing from 3,000 K to 25 K in 12.5 K increments, with dynamics for the smaller of 2 ps or 100 steps ran at each temperature. The NDI moieties were moved as rigid bodies throughout, while the lysine headgroups were given torsion angle degrees of freedom. Non-crystallographic symmetry (NCS) restraints were applied to the K1 portion of each NDI-Lys molecule, specifying that each molecule in a monolayer ring have the same structure as that of every fifth neighbor within each ring. An additional NCS restraint was applied specifying the structure of each monolayer ring be identical to that of its neighbor. If N is the number of molecules in each ring, C_N rotational symmetry was maintained within each ring by the application of distance symmetry restraints between the Nα atoms of K2 for alternating molecules within each ring. Specifically, the distance between molecule i and molecule i+2n+1 was restrained to be the same as that between molecule i and molecule i-(2n+1) for n = 1, …, N/2. Translational symmetry along the tube was maintained using a distance symmetry restraint between one of the oxygen atoms of the NDI moiety in successive rings: the distance of an atom in ring j to the same atom in ring j+1 was restrained to be the same as the distance of atom in ring j to the same atom in ring j-1. To ensure that the NDI-Lys molecules of each monolayer ring lay in the same plane, the distance to plane Xplor-NIH energy term[13] was employed, with the restrained-to planes evenly spaced every 5 Å. The R = 51 Å overall radius of each ring was maintained using a distance restraint between the outermost nitrogen atoms of each NDI moiety to the average position of all the innermost nitrogen atoms for each NDI within the same ring. This radius restraint was reinforced by restraining the intermolecular distances involving four of the aromatic carbon atoms between adjacent molecules in each ring to a distance of $2\pi R/N \pm 0.2$ Å, where N is the number of molecules in each ring. For the flexible K2 lysine headgroups located on the outer surface of the nanotube the C′-Cα-Cβ-Cγ, Cα-Cβ-Cγ-Cδ, and Cβ-Cγ-Cδ-Cε dihedral angles were restrained to values of 180, 180 and 0 ± 5 degrees in order to select one of the possible clusters of low-energy conformers consistent with the experimental intramolecular ^{13}C′-^{13}Cε distance restraint. Finally, a quartic repulsive form was used to enforce atom-atom repulsion.

Quantum Chemical Calculations

Excitonic couplings between pigment molecules are an important factor for studying energy transfer dynamics and interpreting spectroscopic data. Within a first-order approximation, the coupling consists of three terms: Coulomb, exchange, and overlap couplings, all of which can be evaluated in

terms of monomer electronic transition densities.[14,15] In the present work, we also consider the influence of the surrounding medium on the excitonic coupling. The solvent effects on the Coulomb term in condensed media can be introduced using a polarizable continuum model (PCM).[14,16] To compute the coupling values, the transition densities of the monomers in an NDI pair were obtained from a separate calculation on either monomer, followed by evaluation of the coupling integrals between them, along with solvent effects, using Eqs. (17) and (18) in Ref. 16. We used time-dependent density functional theory (TDDFT) with a polarizable continuum model (B3LYP/6-31G*/C-PCM) for these calculations. Geometries for each NDI pair were taken from the nanotube structural model in Fig. 2 with the lysine side chains replaced with methyl groups to reduce cost, a reasonable approximation given that it has previously been shown that the frontier orbitals of analogous perylene diimide chromophores exhibit nodes at the imide nitrogen atoms.[17]

A time scale for excited-state energy transfer between monomer units was estimated based on previously reported time-resolved fluorescence anisotropy (TRFA) measurements,[12] which yield a bi-exponential decay of the fluorescence anisotropy at 410 nm with time constants of 16.6 ps (75.2% amplitude) and 8.7 ps (24.8% amplitude). Since the NDI-Lys monomers cannot tumble freely within the nanotube lattice, we assume that these time scales correspond to energy transfer between monomers rather than their rotational motion. For a set of identical chromophores arranged perfectly around a ring as shown in Fig. 2b, an analytic relationship has been derived[18] that relates the measured depolarization time (τ_{depol}) to the energy transfer or "hopping" time (τ_{hop}):

$$\tau_{depol} = \frac{\tau_{hop}}{4\sin^2\theta}$$

Here, θ is the angle between the transition dipole moment vectors for nearest-neighbor chromophores on the ring. For to the NDI-Lys nanotube structural model containing 52 monomers per ring proposed in this work, $\theta = 360^o/52 = 6.9^o$. Based on this model and the depolarization times measured in the TRFA experiments, we estimate the hopping times τ_{hop} of 0.97 ps and 0.51 ps. Thus, energy transfer in the NDI-Lys nanotube is predicted to occur on a sub-picosecond time scale, even though fluorescence depolarization takes somewhat longer due to the fact that multiple hops are required for a complete loss of anisotropy.

Within the excitonic coupling model, the energy transfer rate depends only on the coupling $k \propto |V|^2$, which is distance-dependent. Figure S8a shows the distance dependence of the coupling along the three nanotube coordinates defined in Fig. 3a, and Fig. S8b converts these coupling constants into distance-dependent rate constants for energy transfer. Highlighted in Fig. S8b is the sub-picosecond energy transfer time scale, which together with the rate constant plots permits the identification of structural parameters for which energy transfer on this time scale is predicted. All three nearest-neighbor distances determined in the NDI-Lys nanotube structural model fall within the sub-ps regime. Importantly, however, there is a range of structural parameters (~4–6 Å in the ring tangent and tube directions, and < 8 Å in the diagonal tangent direction) for which sub-ps energy transfer is expected, suggesting that other materials of this type, exhibiting extremely fast excited-state energy transfer, may be designed via molecular self-assembly.

A nine-NDI subunit of the nanotube structural model was used to examine the extent to which the excitation is delocalized. To avoid artificial low-lying charge-transfer states, the TDDFT calculations employed a long-range corrected (LRC) density functional, LRC-ωPBE.[19] LRC functionals attenuate DFT exchange on a length scale of ~1/ω, replacing it with 100% Hartree-Fock exchange at long distances. The optimal value of the range-separation parameter, ω, depends upon the nature of the exchange-correlation functional and the molecular system,[20-25] but can be optimized in a non-empirical manner so as to satisfy the exact condition IP = $-\varepsilon_{HOMO}$.[25,26] In other words, the highest occupied

molecular orbital (HOMO) energy level should be equal to minus the molecule's ionization potential, as computed using the same functional. An optimal value of $\omega = 0.24$ bohr^{-1} was determined for a single NDI moiety using the LRC-ωPBE functional, where both the neutral monomer and its molecular anion were used in the IP tuning procedure. This functional, with the optimized ω value, was then used in a TDDFT/3-21G* calculation of the nine-NDI unit subsystem. All calculations were performed using a locally modified version of the Q-Chem quantum chemistry package.[27-29] The nature of the excited states was characterized by inspection of the natural transition orbitals (NTOs),[30] which represent the best possible particle/hole representation of a given excited state. Attachment/detachment densities were constructed from the dominant NTOs for visualization of the electron goes upon excitation.

Figure S7 shows the dominant NTOs for the 9-unit model system; the four particle/hole NTO pairs that are shown account for 83% of the transition density, with the remaining 17% distributed amongst a large number of other NTO pairs. The nature of the dominant NTOs is clearly that of coupled π–π* transitions between adjacent dimers, but there is evidence of coupling in various directions within the nanotube.

To examine the extent to which exciton delocalization persists in the presence of structural perturbations, we used the 9-unit model and displaced the monomer units by 1 Å along both of the ring and tube directions, i.e., each monomer is 1 Å farther apart from each of its nearest neighbors than it is in the experimentally-derived structural model. According to Fig. S8a, these structural parameters should still lie within the range where we predict an energy-transfer rate constant consistent with experimental estimates, albeit just barely in the case of the ring-tangent direction. Fig. S9 shows attachment/detachment densities for the lowest optically-allowed transition (S_{27}) in this modified structure. Comparison to the corresponding Fig. 3a for the experimental structure, we see that the wave function remains delocalized across several NDI monomers, albeit in a different way because the relative couplings along the ring, tube, and diagonal directions have changed. Fig. S10 shows the NTOs associated with S_{27} of the modified 9-unit model, and should be compared to Fig. S7 representing the experimentally-derived structure. NTOs for the modified structure continue to paint a picture of excitonic coupling between localized π–π* excitations on the NDI monomers. However, as compared to Fig. S7, where two particular NTO pairs were dominant, in Fig. S10 we see participation by a greater number of NTO pairs (or, if one prefers, a greater number of NDI monomers). This reflects a decrease in the strong coupling in the tube direction, caused by the 1 Å displacement in this direction. Note that some of the delocalization in the more weakly-coupled case (Fig. S9 and S10) is likely somewhat artificially symmetry-driven, and if the effects of thermal fluctuations were included in the model, Fig. S10 especially suggests that the perturbed model is approaching the limit of exciton localization onto a single NDI chromophore.

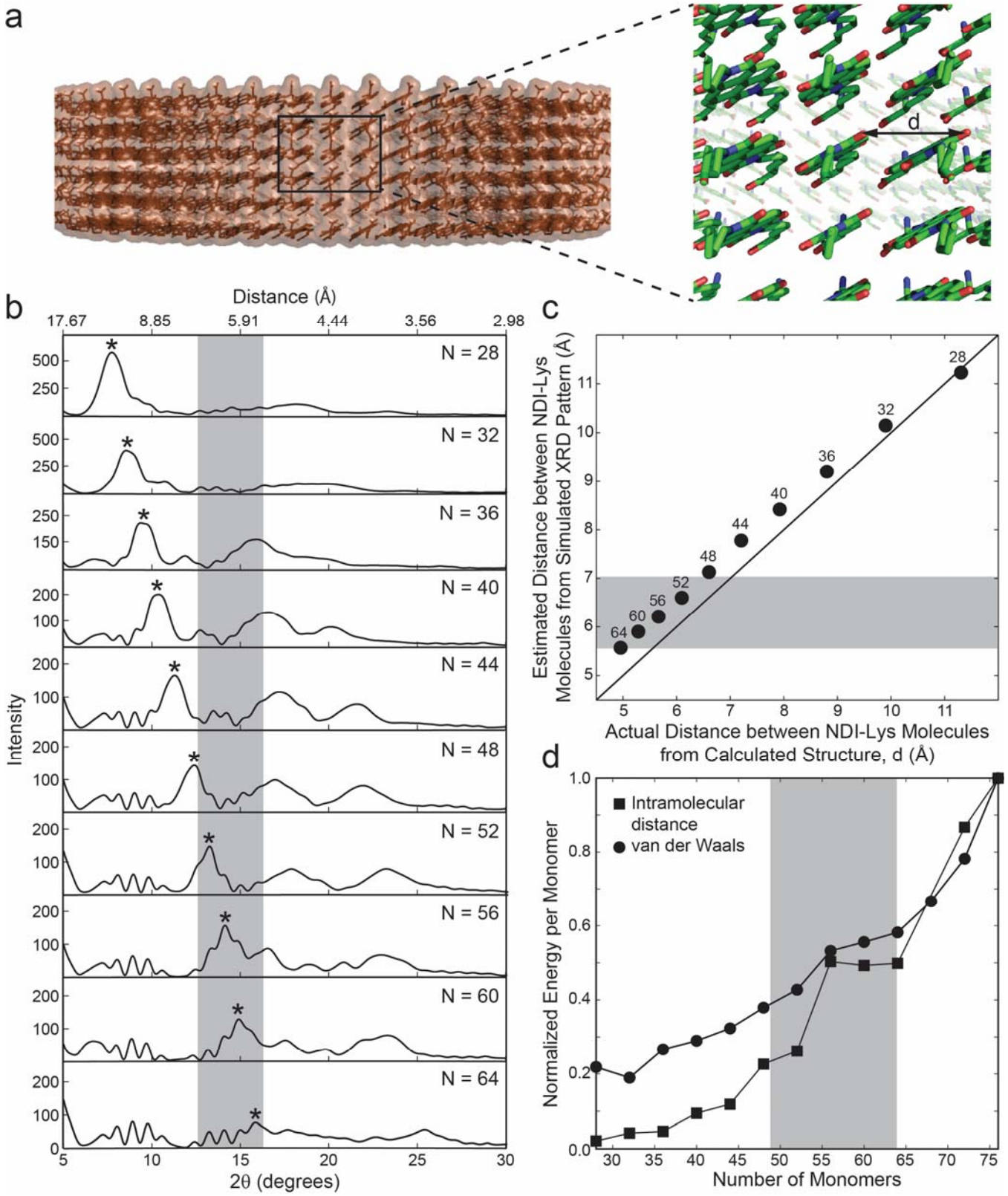
a
d
b
Distance (Å)
17.67
8.85
5.91
4.44
3.56
2.98
N = 28
N = 32
N = 36
N = 40
N = 44
N = 48
N = 52
N = 56
N = 60
N = 64
Intensity
2θ (degrees)
c
Estimated Distance between NDI-Lys Molecules from Simulated XRD Pattern (Å)
Actual Distance between NDI-Lys Molecules from Calculated Structure, d (Å)
28
32
36
40
44
48
52
56
60
64
d
Intramolecular distance
van der Waals
Normalized Energy per Monomer
Number of Monomers

Fig. S1. Estimation of the most likely number of NDI-Lys monomers contained in each monolayer ring based on preliminary nanotube structure calculations and comparison with experimental X-ray powder diffraction and NMR data.[12] **a**, A representative structural model of a nanotube containing six rings calculated in Xplor-NIH using the protocol described in the Methods section, but with the intermolecular K1C′-Nα restraint on distances between adjacent NDI-Lys monomers within a ring omitted. A total of 16 structures were calculated for each type of nanotube with the lowest energy structure from each ensemble used for the subsequent analysis. The distance between the same atoms in adjacent NDI-Lys molecules within a ring, *d*, is indicated in the close-up view. **b-c**, X-ray powder diffraction patterns calculated using the debyer program for structural models obtained with Xplor-NIH for six-ring nanotubes containing increasing numbers of NDI-Lys molecules per ring, *N*, in the 28 and 64 range as indicated (panel **b**). The XRD patterns are displayed as a function of both the scattering angle 2θ and distance, $d = \lambda / (2\sin\theta)$, obtained with the radiation wavelength λ = 1.5418 Å. Note that these XRD calculations were carried out for single nanotubes after first confirming for a test model that the use of lattices of up to 512 nanotubes with random orientations representative of a powder sample produced identical results. These calculations indicate that the position of a major diffraction peak in the XRD patterns (highlighted by an asterisk) is significantly influenced by the number of NDI-Lys monomers contained in a ring, while most other features are relatively invariant with increasing *N*. This peak, which is located at 2θ = ~8° (*d* = ~11 Å) for the 28 monomer per ring model and moves to 2θ = ~16° (*d* = ~5.5 Å) for the 64 monomer per ring model, directly reports on the distance between adjacent NDI-Lys monomers within a ring (c.f., Fig. S3). Indeed, the plot shown in panel **c** reveals a strong correlation between the distance between NDI-Lys monomers within a ring estimated based on the peak position in the simulated XRD pattern and the actual distance between the monomers found in the corresponding structural model calculated in Xplor-NIH (labeled with *d* in the structure in panel **a**). The grey rectangles in panels **b** and **c** indicate the approximate location (position and linewidth) of a relatively broad diffraction peak in the experimental XRD pattern for NDI-Lys nanotubes[12] (c.f., Fig. 2e) interpreted based on the calculated XRD patterns in this study to report on the distance between monomers within a ring. Comparison of the position of this particular feature between the experimental and calculated XRD patterns indicates that the experimental XRD data are consistent with nanotubes containing ~48-64 NDI-Lys monomers per ring. In order to further narrow this range and obtain a single best estimate for the number of monomers per ring, *N*, for the final structure calculations, the magnitudes of the energy terms corresponding to the intramolecular ^{13}C-^{13}C and ^{13}C-^{15}N distances (reporting on the agreement between the experimental distances and corresponding values found in the calculated structures) and repulsive van der Waals interactions (reporting on steric clashes) were inspected for each of the structural models and plotted in panel **d** with the grey bar again indicating the range of NDI-Lys monomers per ring consistent with the XRD data. Note that for reference this plot also includes results of additional calculations for nanotubes with up to 76 monomers per ring, for which calculations of XRD patterns were not performed because the resulting structures displayed significant distortions due to increased molecular crowding and clearly poor agreement with the experimental XRD data based on results of the *N* = 64 calculation. This plot indicates sizeable relative increases in both the intramolecular distance and van der Waals energy terms when the number of monomers per ring is increased from 52 to 56. Therefore, collectively these results suggest that nanotubes containing 52 NDI-Lys molecules per monolayer ring are most consistent with all the experimental XRD and NMR data and yield structural models with acceptable van der Waals repulsion energies.

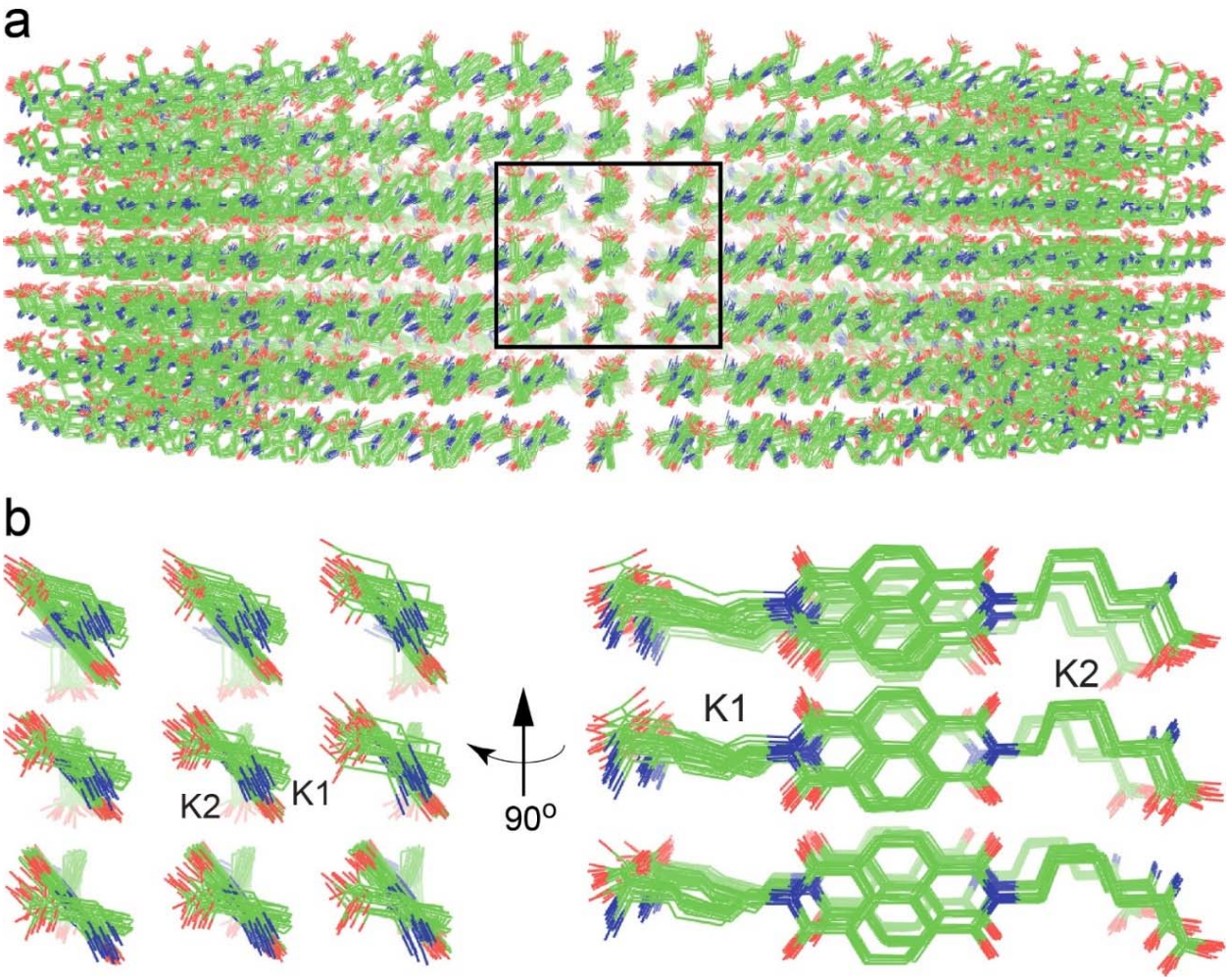

Fig. S2. Ensemble of 20 lowest energy structures of NDI-Lys nanotubes corresponding to the data shown in Fig. 2 of the main text, showing the entire seven ring nanotube (panel **a**) and close up views of a small representative region of the structure extracted from the central three rings (panel **b**).

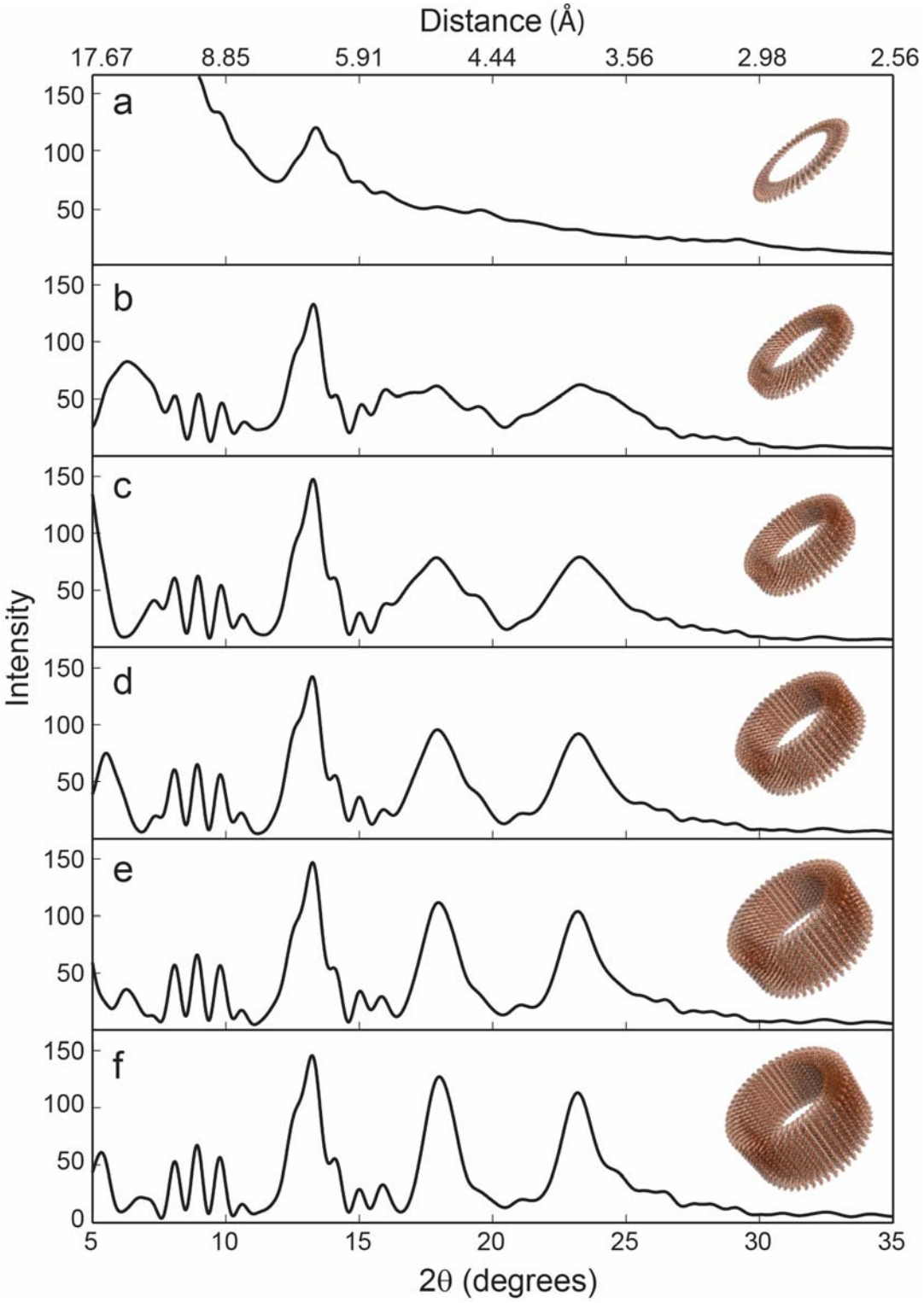

Fig. S3. Investigation of the correspondence between nanotube structural characteristics and features observed in calculated XRD patterns. Nanotube structures were calculated using the protocol described in Fig. S1 caption with 52 NDI-Lys monomers per ring and 1, 4, 6, 8, 10 or 12 rings in panels **a-f**, respectively. The peak at 2θ = ~14° is found in all the calculated patterns and corresponds to the spacing between NDI-Lys molecules within a ring (c.f., Fig. S1). The additional features in the 2θ = ~18-25° regime emerge from the stacking of multiple rings onto one another and become narrower, as expected, with increasing number of rings in the nanotube.

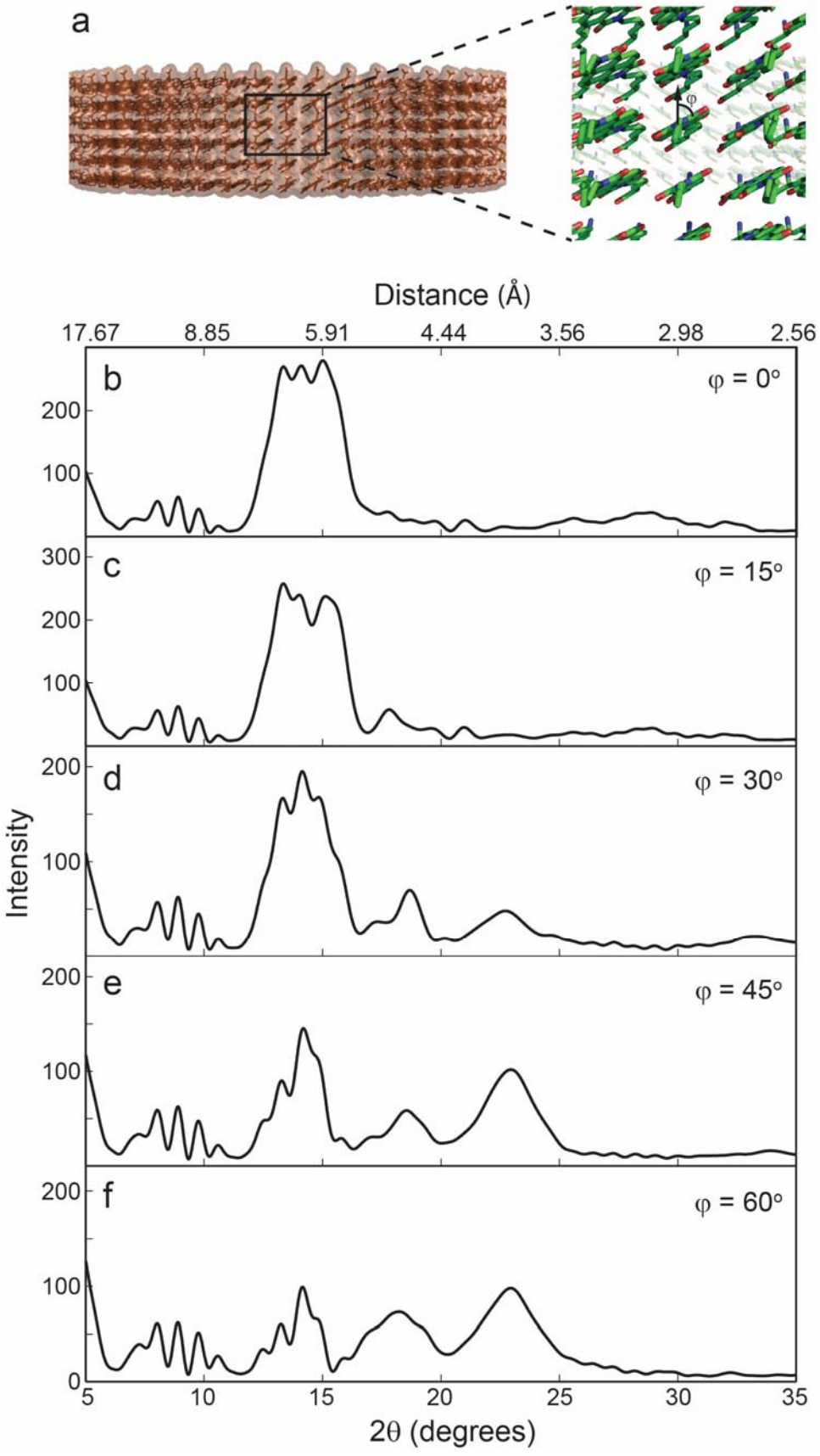
a
φ
Distance (Å)
17.67
8.85
5.91
4.44
3.56
2.98
2.56
b
φ = 0°
c
φ = 15°
d
φ = 30°
e
φ = 45°
f
φ = 60°
Intensity
2θ (degrees)

Fig. S4. Investigation of the correspondence between nanotube structural characteristics and features observed in calculated XRD patterns. For these calculations nanotube structural models were generated with six rings, 52 NDI-Lys monomers per ring, and tilt angles φ for the NDI aromatic moiety within a ring (panel **a**) of 0, 15, 30, 45, 60º in panels **b-f**, respectively. These structural models had the lysine headgroups in an extended conformation and were not subjected to simulated annealing (the precise conformations of the lysines have only a minor influence on the calculated XRD patterns). The key result of this set of calculations is that the presence of diffraction peaks in the 2θ = ~18-25º regime arises from the tilting of NDI-Lys molecules within a ring with the most pronounced features predicted to appear for tilt angles φ > ~15º .

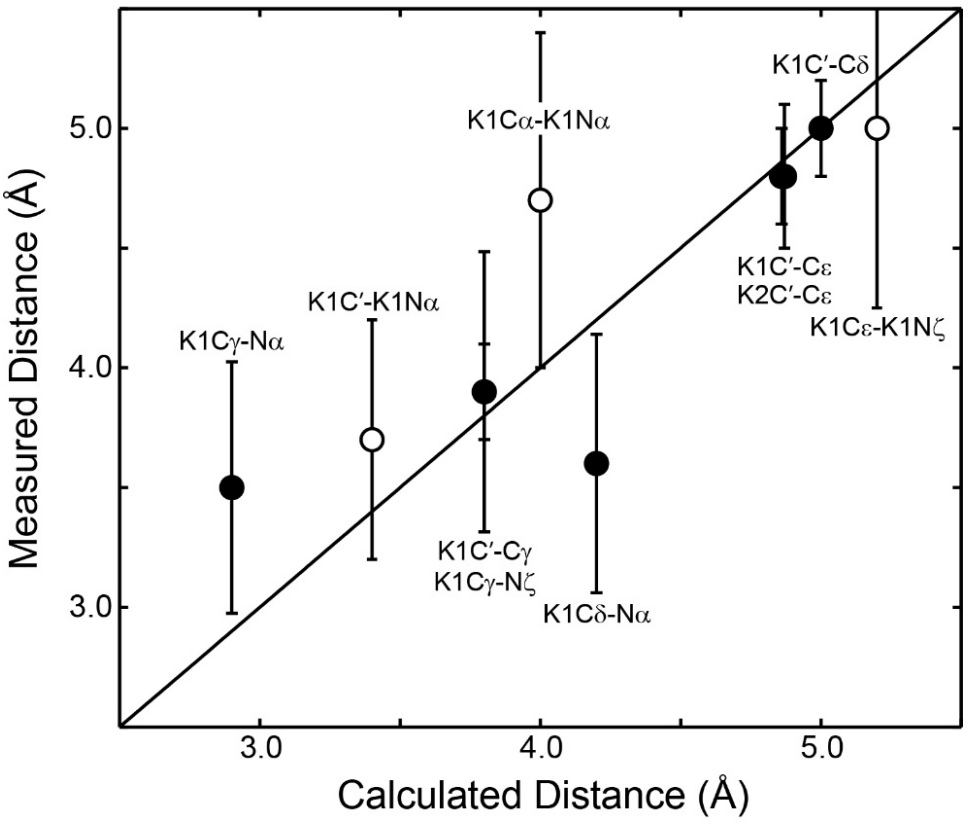

Fig. S5. Comparison of the intramolecular (●) and intermolecular (○) ^{13}C-^{13}C and ^{13}C-^{15}N distances determined by solid-state NMR methods (c.f., Fig. 1 and Table 1) with the corresponding distances in the lowest energy NDI-Lys nanotube structural model shown in Fig. 2. The calculated distances correspond to average values found for several representative monomers located in the central three rings. Uncertainties in the calculated distances were < 0.1 Å and are omitted for clarity.

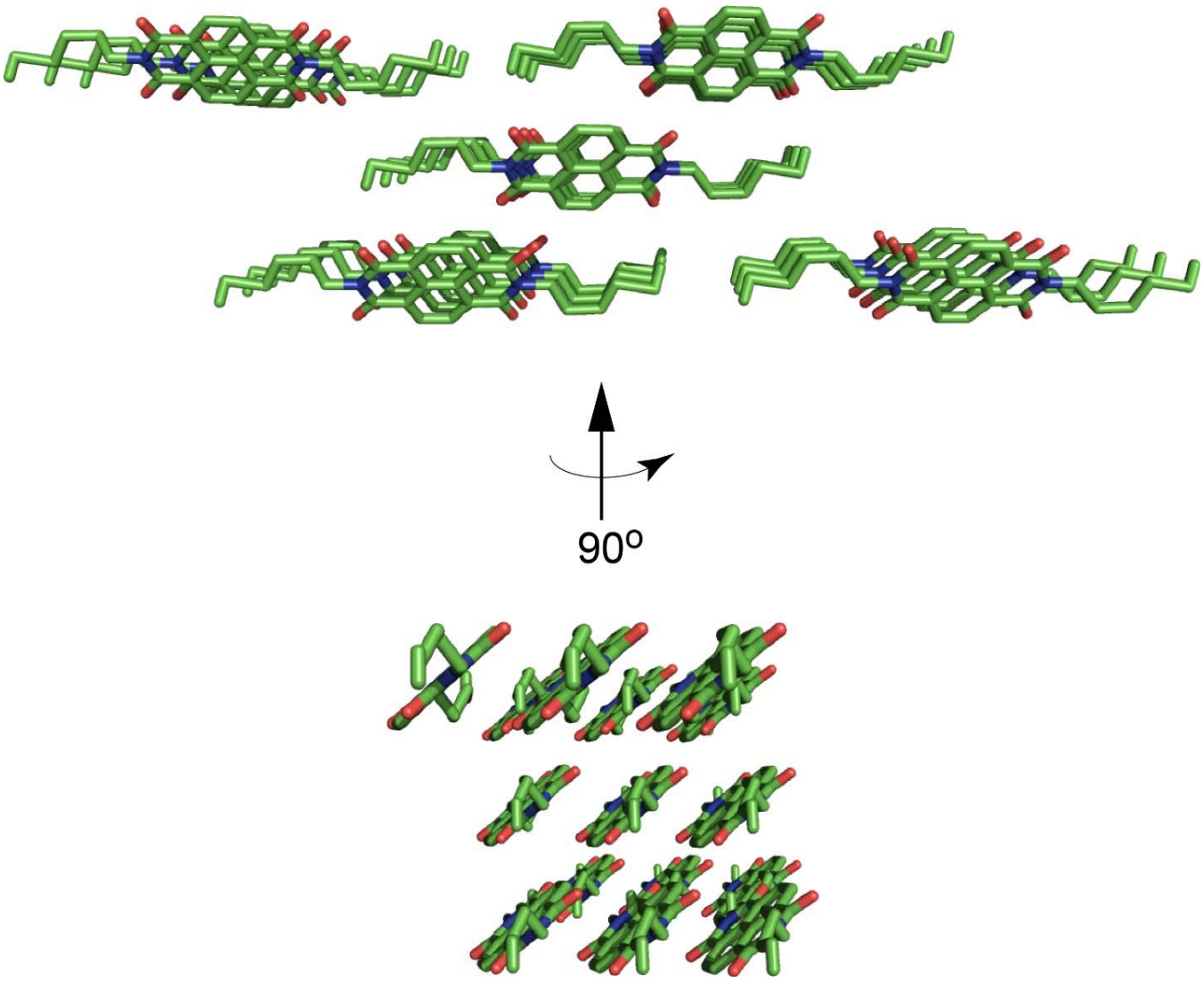

Fig. S6. Two views of the crystal structure of dihexyl-NDI,[31] highlighting structural features that are analogous to those found in this study for the NDI-Lys nanotubes (c.f., Fig. 2).

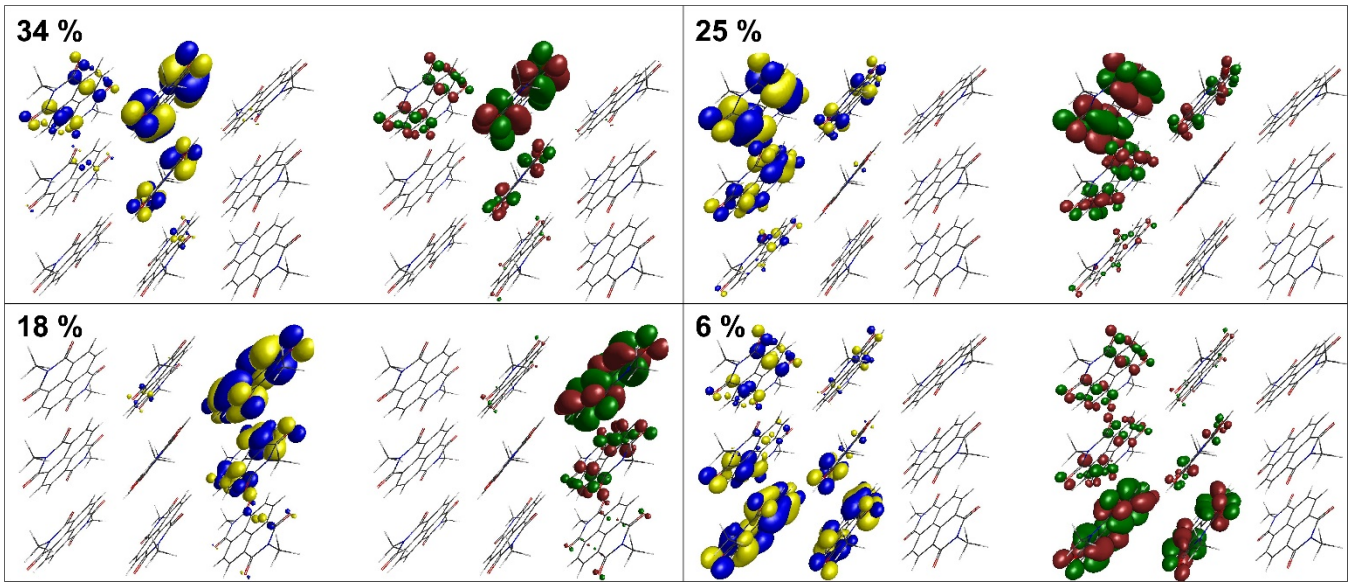

Fig. S7. Dominant natural transition orbitals (NTOs)[30] for the lowest-energy bright state of the nine-NDI unit model system. Each NTO pair consists of an occupied orbital (or hole, upon excitation, which is shown in yellow and blue) and a virtual orbital (or particle, shown in red and green). The excitation is dominated (83% of total amplitude) by excitation energy transfer along the ring direction (c.f., Fig. 3a). The NTOs responsible for this excitation energy transfer are delocalized over dimers in the tube direction.

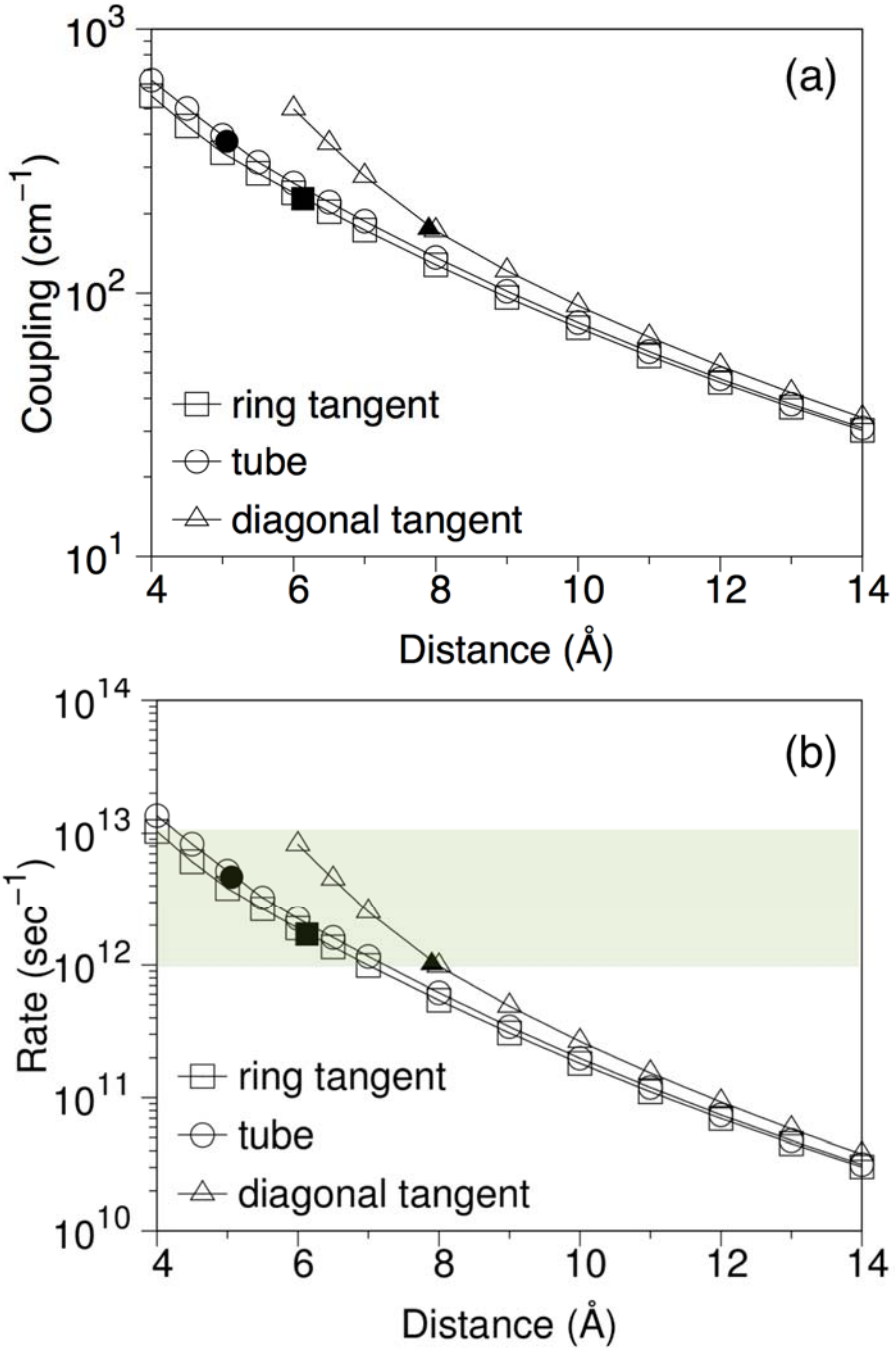

Fig. S8. a, Distance dependence of the excitonic coupling for an NDI dimer that is displaced along the ring, tube, and diagonal directions defined in Fig. 3. Filled symbols represent the distances at the experimentally determined nanotube geometry. The Förster theory result (dipole coupling only) is obtained in the long-distance limit of these plots. **b**, Energy-transfer rate constants computed as a function of distance using the couplings in panel **a**. The shaded region highlights the range of distance parameters for which the model predicts sub-picosecond energy transfer.

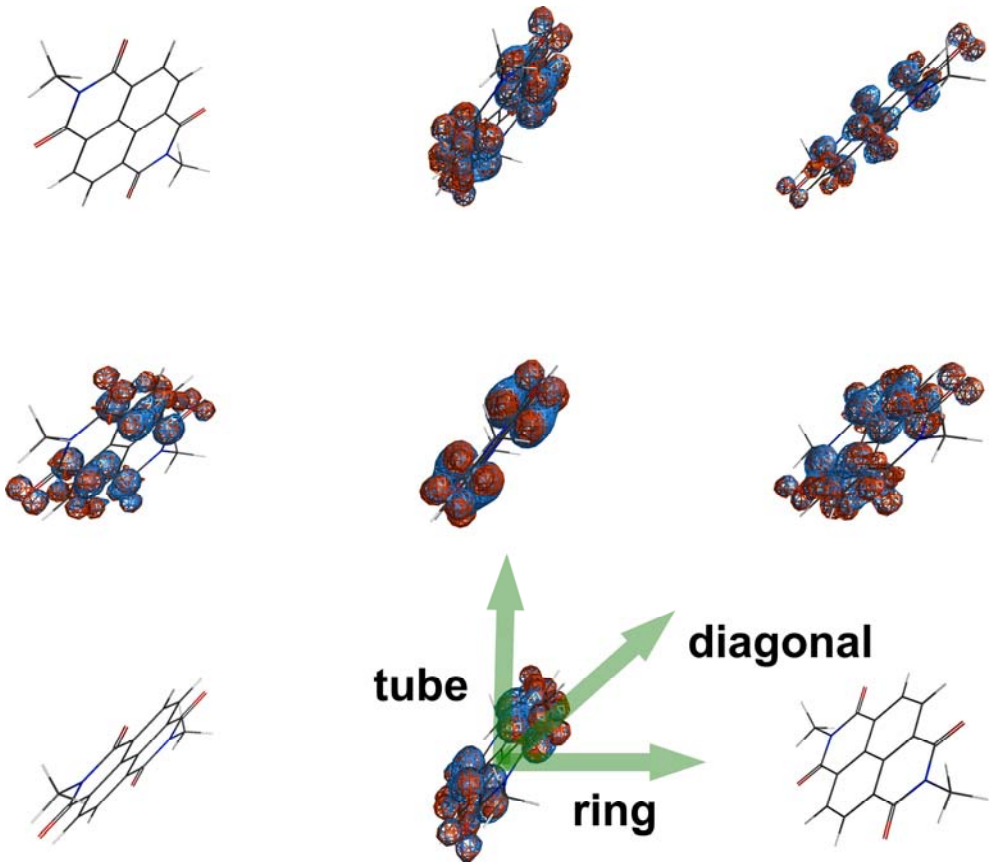

Fig. S9. Quantum chemical calculation of the excited-state wave functions for a 9-unit model whose monomers have been displaced by 1 Å along each of the ring and tube directions. Attachment density (in red) and detachment density (in blue) are shown for the lowest-energy bright state of the model, which should be compared to the corresponding Fig. 3a for the experimentally-derived 9-unit structural model. Delocalization of the excitation remains evident, although the pattern of delocalization is different from that in Fig. 3a.

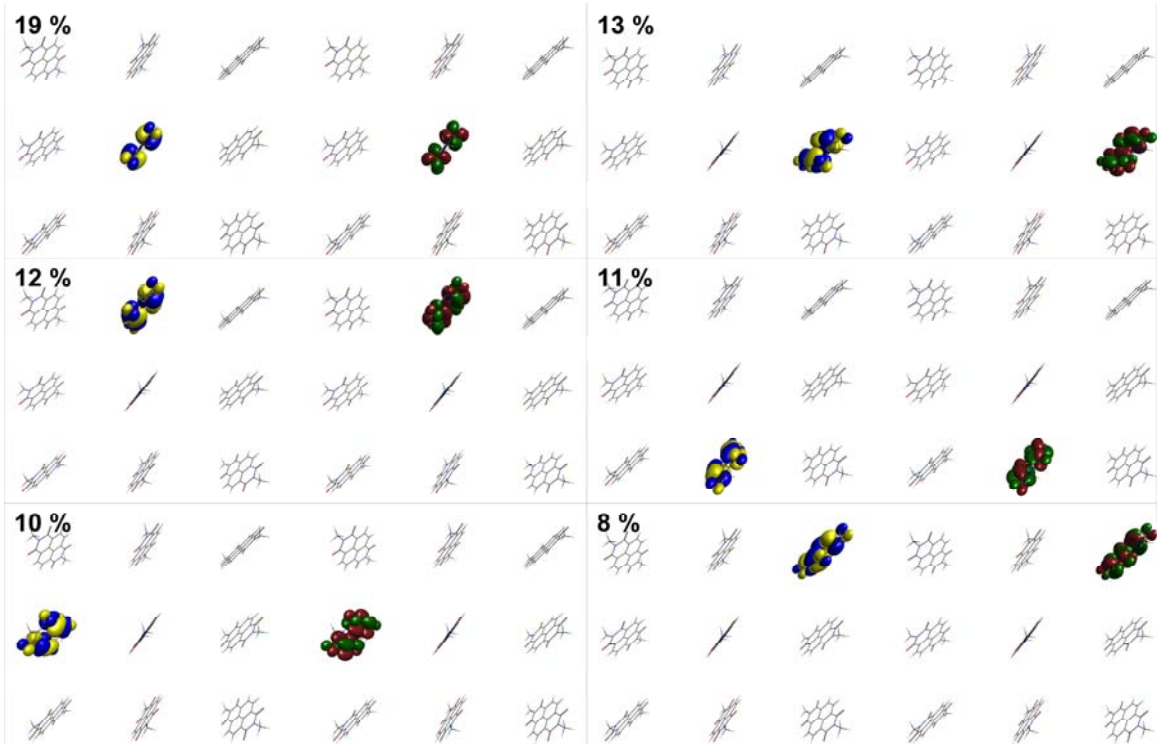

Fig. S10. Dominant NTO pairs for the lowest-energy bright state of the modified structural model in which the monomers have been displaced by 1 Å in both the ring and tube directions. Occupied orbitals (holes) are shown in yellow and blue and virtual orbitals (particles) are shown in red and green. This figure should be compared to the corresponding Fig. S7 for the experimentally-derived 9-unit model. Here, the NTOs that contribute to excitonic delocalization are even more localized on individual NDI chromophores than in Fig. S7. With the diminished strong coupling in the tube direction, this perturbed structure is likely very close to the limit of excitonic localization.

References

(1) Delaglio, F.; Grzesiek, S.; Vuister, G. W.; Zhu, G.; Pfeifer, J.; Bax, A. NMRpipe: A Multidimensional Spectral Processing System Based on Unix Pipes. *J. Biomol. NMR* **1995,** *6*, 277-293.

(2) Helmus, J. J.; Jaroniec, C. P. Nmrglue: An Open Source Python Package for the Analysis of Multidimensional NMR Data. *J. Biomol. NMR* **2013,** *55*, 355-367.

(3) Ramachandran, R.; Ladizhansky, V.; Bajaj, V. S.; Griffin, R. G. ^{13}C-^{13}C Rotational Resonance Width Distance Measurements in Uniformly ^{13}C-Labeled Peptides. *J. Am. Chem. Soc.* **2003,** *125*, 15623-15629.

(4) Raleigh, D. P.; Levitt, M. H.; Griffin, R. G. Rotational Resonance in Solid State NMR. *Chem. Phys. Lett.* **1988,** *146*, 71-76.

(5) Bennett, A. E.; Rienstra, C. M.; Auger, M.; Lakshmi, K. V.; Griffin, R. G. Heteronuclear Decoupling in Rotating Solids. *J. Chem. Phys.* **1995,** *103*, 6951-6957.

(6) Jaroniec, C. P.; Filip, C.; Griffin, R. G. 3D TEDOR NMR Experiments for the Simultaneous Measurement of Multiple Carbon-Nitrogen Distances in Uniformly ^{13}C,^{15}N-Labeled Solids. *J. Am. Chem. Soc.* **2002,** *124*, 10728-10742.

(7) Gullion, T.; Baker, D. B.; Conradi, M. S. New, Compensated Carr-Purcell Sequences. *J. Magn. Reson.* **1990,** *89*, 479-484.

(8) Veshtort, M.; Griffin, R. G. Spinevolution: A Powerful Tool for the Simulation of Solid and Liquid State NMR Experiments. *J. Magn. Reson.* **2006,** *178*, 248-282.

(9) Ye, C.; Fu, R.; Hu, J.; Hou, L.; Ding, S. ^{13}C Chemical Shift Anisotropies of Solid Amino Acids. *Magn. Reson. Chem.* **1993,** *31*, 699-704.

(10) Helmus, J. J.; Surewicz, K.; Apostol, M. I.; Surewicz, W. K.; Jaroniec, C. P. Intermolecular Alignment in Y145stop Human Prion Protein Amyloid Fibrils Probed by Solid-State NMR Spectroscopy. *J. Am. Chem. Soc.* **2011,** *133*, 13934-13937.

(11) Debye, P. Zerstreuung Von Röntgenstrahlen. *Ann. Phys.* **1915,** *351*, 809-823.

(12) Shao, H.; Seifert, J.; Romano, N. C.; Gao, M.; Helmus, J. J.; Jaroniec, C. P.; Modarelli, D. A.; Parquette, J. R. Amphiphilic Self-Assembly of an N-Type Nanotube. *Angew. Chem. Int. Ed.* **2010,** *49*, 7688-7691.

(13) Xu, C.; Gagnon, E.; Call, M. E.; Schnell, J. R.; Schwieters, C. D.; Carman, C. V.; Chou, J. J.; Wucherpfennig, K. W. Regulation of T-Cell Receptor Activation by Dynamic Membrane Binding of the Cd3ε Cytoplasmic Tyrosine-Based Motif. *Cell* **2008,** *135*, 702-713.

(14) Hsu, C.-P.; Fleming, G. R.; Head-Gordon, M.; Head-Gordon, T. Excitation Energy Transfer in Condensed Media. *J. Chem. Phys.* **2001,** *114*, 3065-3072.

(15) You, Z.-Q.; Hsu, C.-P. Theory and Calculation for the Electronic Coupling in Excitation Energy Transfer. *Int. J. Quantum Chem.* **2014,** *114*, 102-115.

(16) Iozzi, M. F.; Mennucci, B.; Tomasi, J.; Cammi, R. Excitation Energy Transfer (EET) between Molecules in Condensed Matter: A Novel Application of the Polarizable Continuum Model (PCM). *J. Chem. Phys.* **2004,** *120*, 7029-7040.

(17) Würthner, F. Perylene Bisimide Dyes as Versatile Building Blocks for Functional Supramolecular Architectures. *Chem. Commun.* **2004**, 1564-1579.

(18) Jimenez, R.; Dikshit, S. N.; Bradforth, S. E.; Fleming, G. R. Electronic Excitation Transfer in the LH2 Complex of Rhodobacter Sphaeroides. *J. Phys. Chem.* **1996,** *100*, 6825-6834.

(19) Rohrdanz, M. A.; Martins, K. M.; Herbert, J. M. A Long-Range-Corrected Density Functional That Performs Well for Both Ground-State Properties and Time-Dependent Density Functional Theory Excitation Energies, Including Charge-Transfer Excited States. *J. Chem. Phys.* **2009,** *130*, 054112.

(20) Baer, R.; Neuhauser, D. Density Functional Theory with Correct Long-Range Asymptotic Behavior. *Phys. Rev. Lett.* **2005,** *94*, 043002.
(21) Bylander, D. M.; Kleinman, L. Good Semiconductor Band Gaps with a Modified Local-Density Approximation. *Phys. Rev. B* **1990,** *41*, 7868-7871.
(22) Savin, A.; Flad, H.-J. Density Functionals for the Yukawa Electron-Electron Interaction. *Int. J. Quantum Chem.* **1995,** *56*, 327-332.
(23) Livshits, E.; Baer, R. A Density Functional Theory for Symmetric Radical Cations from Bonding to Dissociation. *J. Phys. Chem. A* **2008,** *112*, 12789-12791.
(24) Krukau, A. V.; Scuseria, G. E.; Perdew, J. P.; Savin, A. Hybrid Functionals with Local Range Separation. *J. Chem. Phys.* **2008,** *129*, 124103.
(25) Livshits, E.; Baer, R. A Well-Tempered Density Functional Theory of Electrons in Molecules. *Phys. Chem. Chem. Phys.* **2007,** *9*, 2932-2941.
(26) Stein, T.; Kronik, L.; Baer, R. Reliable Prediction of Charge Transfer Excitations in Molecular Complexes Using Time-Dependent Density Functional Theory. *J. Am. Chem. Soc.* **2009,** *131*, 2818-2820.
(27) Shao, Y.; Molnar, L. F.; Jung, Y.; Kussmann, J.; Ochsenfeld, C.; Brown, S. T.; Gilbert, A. T.; Slipchenko, L. V.; Levchenko, S. V.; O'Neill, D. P. et al. Advances in Methods and Algorithms in a Modern Quantum Chemistry Program Package. *Phys. Chem. Chem. Phys.* **2006,** *8*, 3172-3191.
(28) Krylov, A. I.; Gill, P. M. W. Q-Chem: An Engine for Innovation. *WIREs Comput. Mol. Sci.* **2013,** *3*, 317-325.
(29) Shao, Y.; Gan, Z.; Epifanovsky, E.; Gilbert, A. T. B.; Wormit, M.; Kussmann, J.; Lange, A. W.; Behn, A.; Deng, J.; Feng, X. et al. Advances in Molecular Quantum Chemistry Contained in the Q-Chem 4 Program Package. *Mol. Phys.* **2015,** *113*, 184-215.
(30) Martin, R. L. Natural Transition Orbitals. *J. Chem. Phys.* **2003,** *118*, 4775-4777.
(31) Shukla, D.; Nelson, S. F.; Freeman, D. C.; Rajeswaran, M.; Ahearn, W. G.; Meyer, D. M.; Carey, J. T. Thin-Film Morphology Control in Naphthalene-Diimide-Based Semiconductors: High Mobility N-Type Semiconductor for Organic Thin-Film Transistors. *Chem. Mater.* **2008,** *20*, 7486-7491.